Proceedings of the 16th European Turbomachinery Conference (ETC16)
Turbomachinery, Fluid Dynamics and Thermodynamics,
March 24-28, 2025; Hannover, Germany

Direct Numerical Simulations of the SPLEEN cascade: a study of the impact of compressibility on transition and separation in a low-pressure turbine passage

Maxime Borbouse[1], Deneffe Nathan[1], Thys Mars[1], Margaux Boxho[2], Michel Rasquin[2], Gustavo Lopes[3], Sergio Lavagnoli[3], and Koen Hillewaert*[1,2,3]

[1]Department of Aerospace and Mechanics, University of Liège, Allée de la Découverte, 9, 4000 Liège, Belgium
[2]Cenaero, Rue des Frères Wright 29, 6041 Charleroi, Belgium
[3]Turbomachinery Department, von Karman Institute for Fluid Dynamics, Chaussée de Waterloo 72, 1640 Rhode-Saint-Genèse, Belgium

Abstract

A detailed experimental analysis of the flow in a representative high-speed low pressure turbine cascade, dubbed SPLEEN C1, was undertaken in the framework of the SPLEEN project. The latter is supplemented by a Direct Numerical Simulation campaign in view of interpreting the observed flow. The simulations are undertaken using ArgoDG, a high order discontinuous Galerkin code developed at Cenaero, which has been *a.o.* equipped for studying cascade flows. This paper presents subsonic ($M_{s,out} = 0.7$), transonic ($M_{s,out} = 0.9$) and choked conditions ($M_{s,out} = 0.95$) at two different Reynolds numbers ($Re_{s,out} = 70 \times 10^3$ and 120×10^3) without inlet turbulence. Visualisations of the flow are provided through Mach contours and numerical Schlieren. Numerical and experimental results are compared based on pressure and skin friction distribution as well as boundary layer state and losses. The impact of compressibility is highlighted, suppressing the separation on the suction side for choked conditions. Choking also prevents acoustic perturbations to propagate upstream. Separation and transition on the pressure side develop independently.
Keywords: LPT, GTF, DNS, shock, turbulence, separation

1 Introduction

In the context of the ongoing energy transition of aviation industry, reducing the environmental impact of air travel has become a central focus. This transition requires innovative propulsion technologies, with turbofan engines playing a pivotal role in enhancing fuel efficiency. The challenge of improving both thermodynamic and propulsive efficiency is well recognized. While material limitations restrict advancements in thermodynamic efficiency, Kurzke [1] showed that propulsive efficiency can be further improved by increasing the engine bypass ratio.

In conventional turbofans, the fan is directly mounted on the low-pressure (LP) spool, restricting fan rotation speeds to avoid excessive shock losses. This limitation results in lower LP turbine (LPT) speeds and higher stage counts. The geared turbofan (GTF) concept overcomes this by allowing the fan and LP spool to rotate at different speeds, leading to a *high-speed LPT* (HSLPT) that operates at significantly higher speeds, enhancing work per stage and reducing the number of stages. Consequently, this innovation lowers specific fuel consumption (SFC), reduces engine weight, and improves overall fuel efficiency (see Kurzke [1]).

Classical LPTs have been extensively studied in their nominal and extra-nominal conditions. However, there remains a gap in the data and open-source studies concerning HSLPTs.

HSLPTs operate at low Reynolds numbers and transonic velocities, where compressibility effects significantly influence profile loss. One of the main contributors to profile loss is suction-side (SS) boundary layer (BL) separation due to the potential laminar boundary layer separation [2, 3]. Turbulence generated by wake interactions can help alleviate these losses thanks to small *separation bubble*, *i.e.*, wherein the flow detaches from the surface due to a relatively important adverse pressure gradient (ADG), then reattaches in virtue of turbulence and a stronger BL momentum [4–10]. Understanding the behavior of separation bubbles and the associated transition phenomena is crucial for optimizing LPT performance. Transition can occur via multiple pathways, *a.o.* natural transition, bypass and wake-induced. Numerous studies have investigated separation bubbles and transition in both flat plates and LPT environments [2, 11–13]. Schubauer and Klebanoff [14] conducted a study of contributions on the mechanics of boundary-layer transition.

In LPTs, separation bubbles are prone to the *bubble bursting* phenomenon, where they oscillate between short and long laminar bubble modes. This behavior has been extensively studied in recent works such as Dellacasagrande et al. [15] and Dellacasagrande et al. [16].

Furthermore, both Mach number [17–20] and Reynolds number [21] play key roles in LPT performance. With increasing Reynolds number, Vera et al. [17] showed the losses decrease faster for HSLPT rather than their low speed counterparts while they increase with the Mach number. Additionally, compressibility effects can strongly impact both separation and transition phenomena. Notably, Börner and Niehuis [22] showed that the normal shock amplifies boundary layer transition over the separation bubble, causing downstream reattachment, with low-frequency shock oscillations and boundary layer instabilities observed in Schlieren images and Surface Hot-Film sensor data.

The loss generation mechanisms in turbine cascades have been studied by a number of authors. Through a momentum

*Corresponding author: koen.hillewaert@cenaero.be

Paper ID: ETC2025-282

balance, Denton [23] introduced a conceptual breakdown in contributions by the boundary layer, the base flow and potentially open separation. Sieverding and Manna [24] performed a review of TE flows in turbomachinery flows. Vagnoli et al. [25] conducted a study in which they presented TE wake flow (base flow) characteristics and compared them to experimental data. Through LES simulations, they proved that, with increasing Mach number, the TE base pressure transitions from a uniform distribution at moderate subsonic speeds to a progressively stronger non-uniform profile in the transonic range, before abruptly returning to an isobaric state.

From a numerical perspective, traditional methods such as Reynolds averaged Navier-Stokes (RANS), unsteady Reynolds averaged Navier-Stokes (URANS), and to a lesser extent Large Eddy Simulations (LES) encounter difficulties in accurately capturing the interaction between transition, separation, shocks and flow interactions [26]. While transition-sensitive turbulence models have been developed [27–29], high-fidelity simulations like direct numerical simulation (DNS) are necessary to fully resolve the complexities of these flows [30]. Advances in high-performance computing (HPC) and the use of higher-order methods, such as the discontinuous Galerkin method (DGM), have made DNS feasible for turbomachinery applications.

This work is part of the SPLEEN project, led by the von Karman Institute for Fluid Dynamics (VKI) in collaboration with Safran Aircraft Engines and the University of Liège and the support of Cenaero. The project investigates the aerodynamics of HSLPTs under the influence of unsteady wakes and purge flows, with a focus on on- and off-design conditions in geared turbofan engines. Three cases will be considered: the first involves a clean inlet flow, the second introduces turbulence injection, and the last case integrates rotating bars in front of the passage. The reason behind the several approaches is to be able to decouple the different physical phenomena, *e.g.*, separation and transition, from their cause, *i.e.*, the blade itself, the turbulence or the wake passage. This process also allows to assess the interactions between the different effects and contributions. The current paper discusses, as a first step, the clean conditions in detail, whereas the turbulent inflow and wake cases will be presented in follow-up papers. Experimental results from Lopes et al. [31], Lopes et al. [32, 33], and Simonassi et al. [34], gathered in the open-source database [35], are compared with DNS simulations [36, 37]. Note that PIV experimental measurements extracted in the scope of the same project are also analysed in Okada et al. [38].

2 Numerical setup

A deep understanding of turbomachinery flows requires access to the detailed flow. Notably, the results should accurately represent turbulent structures developing in the BL and in the wake, shear layers, compressibility and shocks and the interactions between these phenomena. To achieve this, the solver *ArgoDG* [39] of Cenaero, based upon the discontinuous Galerkin Method (DGM), is used. DGM combines advantages of finite elements method (FEM) and finite volumes method (FVM) making it respectively attracting for its high accuracy on unstructured meshes and its conservation and stability properties for convection-dominated problems. DGM implemented in Argo was validated for DNS of transitional flows in [40] and has been employed to investigate various complex flow regimes, including transonic flows [41], transitional turbomachinery flows [42–44], and shock-dominated turbomachinery flows [45]. The computations presented in this work have been performed on *Lucia*, the Tier-1 HPC supercomputer of the Walloon Region, operated by Cenaero. The mesh was constructed using Gmsh [46], while visualization and post-processing were carried out using ParaView along with a dedicated plugin designed for high-order meshes—*i.e.*, composed of curved elements—and high-order polynomial solutions [47].

2.1 Numerical model and solver parameters

The spatial discretisation is based on a 4th order DGM. The symmetric interior penalty (SIP) term is used to stabilize the diffusive term. It is to be noted that no shock capturing strategy was used. Time-integration is performed using an implicit second order backwards difference (BDF2) scheme. The system is solved with a Newton-GMRES (generalized minimal residual) method, preconditioned with a single precision block Jacobi preconditioner. In order to prevent wave reflection on the domain outlet, a sponge layer with a spatially varying strength is added. Note that the leading edge (LE) is fixed at the origin of the coordinate system such that the sponge layer is located $2.25 \times c_{\mathrm{ax}}$ downstream the trailing edge (TE).

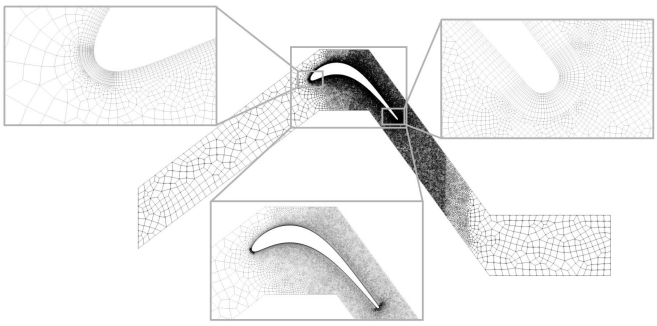

Figure 1: Computational domain and mesh.

Table 1: Geometric parameters.

Parameter	Symbol	Value	Units
True chord	c	52.28	mm
Axial chord	c_{ax}	47.61	mm
Pitch	g	32.95	mm
Span	z	165	mm
TE radius	$d_{\mathrm{TE}}/2$	0.435	mm
Throat opening	o	19.4	mm
Inlet angle	$\beta_{\mathrm{m,in}}$	37.3	deg
Outlet angle	$\beta_{\mathrm{m,out}}$	53.8	deg
Stagger angle	ζ	24.4	deg

The fluid properties are assumed to be those of an ideal gas, with a specific heat ratio $\gamma = 1.4$ and a gas constant $R =$

Table 2: Boundary conditions for all the numerical cases. Reynolds and Mach numbers refer to the outlet isentropic quantities.

Parameter	Symbol	Value						Units
Reynolds number	$\mathrm{Re}_{s,out}$	70×10^3			120×10^3			-
Mach number	$M_{s,out}$	0.7	0.9	0.95	0.7	0.9	0.96	-
Inlet total pressure	$p_{0,in}$	10779.39	9500.24	9318.31	18478.96	16286.13	15920.44	Pa
Outlet static pressure	p_{out}	7771.16	5617.12	5213.22	13322	9629.34	8806.7	Pa
Inlet total temperature	$T_{0,in}$		300			300		K
Flow angle	α		36.3			36.3		deg

$287.06\,\mathrm{J\,kg^{-1}\,K^{-1}}$. Viscosity and conductivity are computed using Sutherland's law.

The computations were performed for two outlet isentropic Reynolds numbers of $\mathrm{Re}_{s,out} = 70 \times 10^3$ (referred to as "low") and 120×10^3 ("high") and for three outlet isentropic Mach numbers of $M_{s,out} = 0.7$ (referred to as "subsonic"), 0.9 ("transonic") and 0.95 ("supersonic")[1].

The time step is $\Delta t = 0.1$ µs for all cases except for the case $\mathrm{Re}_{s,out} = 120 \times 10^3$ and $M_{s,out} = 0.7$ for which it was reduced to $\Delta t = 0.05$ µs.

2.2 Computational domain

The computational domain and mesh are shown in Figure 1 and the geometric parameters are given in Table 1.

The computational domain is periodic in both the spanwise and pitchwise direction. A single pitch is considered, whereas a spanwise extent of 7% of c is considered. The in- and outlet boundaries of the domain are set far enough from the blade in such a way that the flow remains the least affected by the corresponding boundary conditions. More precisely, the inlet boundary is set at a distance of $2 \times c_{ax}$ from the LE and the outlet at a distance of $2.4 \times c_{ax}$ of the TE, which allows to analyse the wake in a larger region.

2.3 Boundary conditions

No-slip adiabatic conditions are enforced at the blade surface, total conditions and flow angles at the inlet and static pressure at the outlet. Finally, let us recall that the presented computations were performed without any turbulence injection. The imposed values, listed in Table 2, are derived from the experimental studies [31–34].

2.4 Refinement zones and wall resolution

The mesh was constructed in order to achieve a high spatial resolution while keeping a reasonable computational cost.

The mesh is unstructured far from the blade and contains a structured O-type boundary layer mesh up to a distance of 1.45% of c from the blade. The mesh is refined near the LE and near the TE, where the element size is of 0.08% of c, and in the base region, where the element size is of 0.76% of c. The passage, from LE to $1.5 \times c_{ax}$, is characterised by an element size of 0.15% of c and by a maximum element size of 7.5% of c. The base flow refinement zone, from TE to 50% of c_{ax}, is identified by a reference cell size of 0.75% of c. The cells adjacent to the blade surface are curved elements of order 2 with a resolution of order 3. The mesh is ultimately extruded in the z-direction using 10 layers over a distance corresponding to 7% of the chord length c.

[1] The outlet isentropic Mach number for the choked high Reynolds case is 0.96 rather than 0.95.

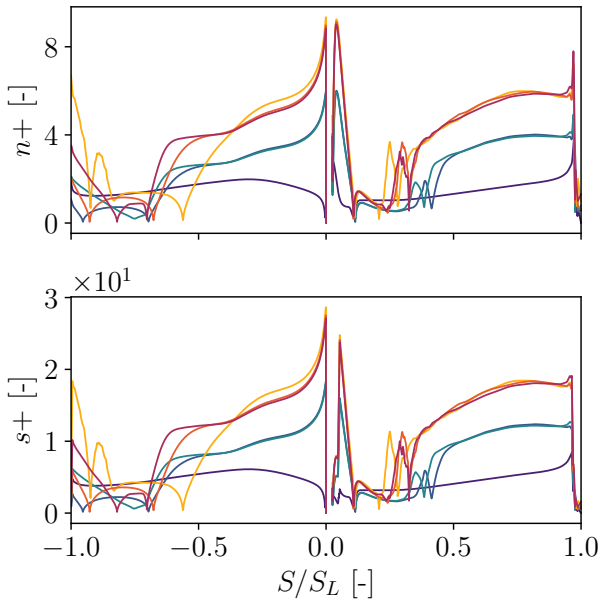

Figure 2: Wall normal n^+ and wall-tangential resolution s^+ in wall units. Negative abscissa correspond to the PS while positive abscissa correspond to SS. Legend: $\mathrm{Re}_{s,out} = 70$k and $M_{s,out} = 0.7$; $\mathrm{Re}_{s,out} = 70$k and $M_{s,out} = 0.9$; $\mathrm{Re}_{s,out} = 70$k and $M_{s,out} = 0.95$; $\mathrm{Re}_{s,out} = 120$k and $M_{s,out} = 0.7$; $\mathrm{Re}_{s,out} = 120$k and $M_{s,out} = 0.9$; $\mathrm{Re}_{s,out} = 120$k and $M_{s,out} = 0.95$.

For DNS, one generally wants a resolution in wall units of about 10 in the streamwise direction, 5 in the spanwise and 1 in the normal direction. The normal mesh size in the boundary layer is 0.38% of c next to the blade, corresponding to a wall normal resolution in wall units $n^+ \leq 8$, whereas an exponential cell growth rate of 1.2 is used. Due to the high-order resolution, this corresponds to actual values of $n^+ \leq 2.7$ and $\sqrt[3]{1.2}$ respectively. Given the need to resolve separation and reattachment, the resolution in stream- and spanwise direction was chosen to be equal. The wall resolution corresponding to the cell size is provided in Figure 2, with n^+ corresponding to the wall-normal and s^+ the wall-tangential resolution. Except for the leading edge, the tangential resolution remains well below 20, which, in view of the high-order resolution and the cubic interpolation, is deemed sufficient

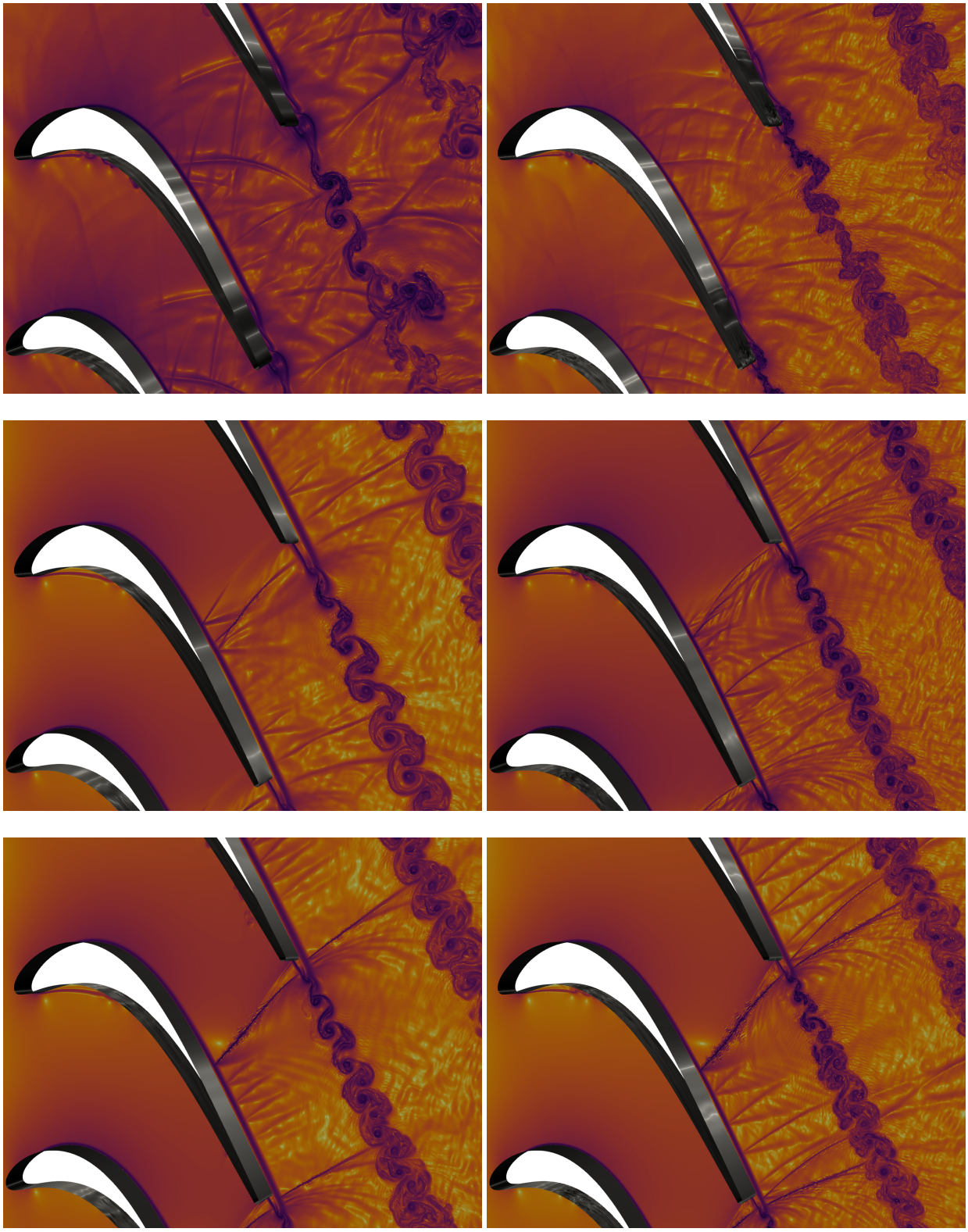

Figure 3: Snapshots of numerical Schlieren in the domain and wall shear stress contours along the blade for $\mathrm{Re}_{s,out} = 70 \times 10^3$ to 120×10^3 from left to right, respectively, and $M_{s,out} = 0.7$, 0.9, 0.95 (resp. 0.96) from top to bottom, respectively. Color maps are displayed in logarithmic scale.

The final mesh presented in Figure 1 is composed of 5337 hexahedra and 16981 two-dimensional quadrangles.

3 Results

This section presents the DNS results against experimental measurements when available.

3.1 Flow visualisation

The flow visualisations shown in Figure 3 provide snapshots of the numerical Schlieren shadowgraph ($||\boldsymbol{\nabla}\rho||/\rho$) in the periodic plane, combined to the shear stress norm on the blade.

The Schlieren graph reveals acoustic perturbations that propagate upstream, created by the vortex shedding in the base flow. In the subsonic case, these perturbations reach far upstream up to the LE region. They are reflected on the blade surface, forming "V" shaped wave trains in the flow. The presence of a supersonic region close to the throat prevents this behavior for the transonic case and especially in the choked case. One may notice a more stable von Karman street for higher Mach numbers, while it is disordered in subsonic conditions.

The wall shear stress along the blade is shown as well in Figure 3. An interesting observation concerns the high Reynolds subsonic case: the flow is already relatively chaotic in the TE region. Flow separation clearly occurs on the PS for all cases and along the SS only in subsonic and transonic conditions.

3.2 Blade loading

The mean isentropic Mach distributions along the blade are shown in Figure 4.

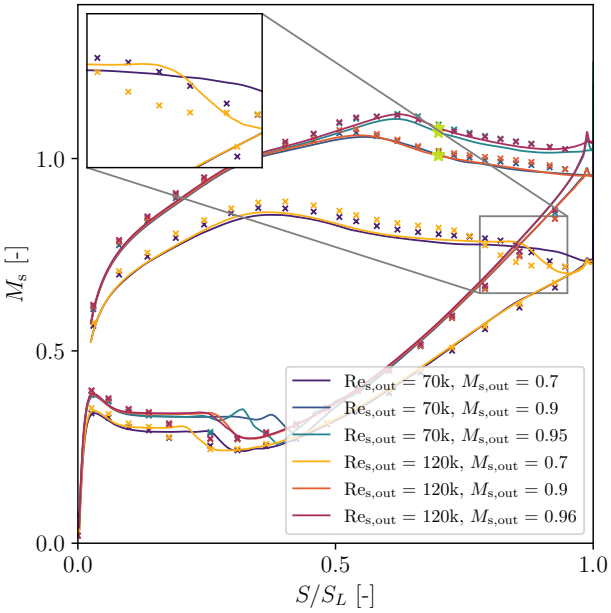

Figure 4: Time and spanwise averaged isentropic Mach number distributions along PS (lower curves) and SS (upper curves) for $\mathrm{Re}_{s,out} = 70 \times 10^3$ to 120×10^3, and $M_{s,out} = 0.7$, 0.9, 0.95 (resp. 0.96). Experimental measurements are represented by cross ($\times$) symbols. The averaged shock location is represented by $\star$.

The distributions on the PS are all characterized by a plateau, between $S/S_L \approx 0.1$ and 0.3, which is not observed in the experiments. According to the authors, this behavior may be attributed to the absence of turbulence at the inlet in the computations, while the measured turbulence intensity is at least about 2.5%. This may affect the turbulent mixing, thus impacting separation and reattachment (location). Moreover, the chaotic behavior of the flow seen in Figure 3 is much higher in the subsonic cases, having an impact on the length of the separation bubble. Again, the lower turbulence level in the numerical simulations leads to a lower turbulent spot production, which lengthens the transition. This hypothesis is supported by the fact that, at higher Reynolds numbers, the bubble narrows further. The separation bubbles can also be observed in the visualisations of Figure 3. The numerical and experimental results are well matched for the rear part of the PS. Nevertheless, it must be noted that no definitive conclusion can be drawn from the latter discussion, as the results with inlet turbulence are not presented here and will be included in future communications.

Distributions along the SS match the experimental results rather well for the transonic and choked cases. A small anomaly is however observed for the low Reynolds subsonic case between $S/S_L = 0.5$ and 0.9, which is explained by the presence of a separation bubble, also visible in Figure 3. Furthermore, the pressure recovery observed in the experimental results does not match the numerical one. Moreover, small discrepancies in the reattachment region appear at low Mach number, which are larger at high Reynolds number. Again, the latter differences could be due to the zero-inlet turbulence in the numerical setup, according to the authors.

The effect of an increased Mach number is to shift the velocity peak downstream. For this reason, the adverse pressure gradient develops on a smaller part of the blade as the Mach number increases. In contrast, due to the very similar growth along the nose part of the blade SS up to the suction peak, the pressure rise between the velocity peak and the TE is smaller than one could expect. On the other hand, the effect of increasing the Reynolds number is felt more at low Mach number. In particular, one can observe a separation bubble at the rear part of the SS, indicated by the plateau followed by a small pressure recovery. This pressure recovery is always present in experimental data. Additionally, this separation bubble appears more upstream in experimental measurements.

The lower loading from the LE to the laminar separation may be attributed to a longer evolution of the separation bubble due to the absence of inlet turbulence: a large separation bubble can trigger the modification of the loading up to the LE [2, 48, 49].

3.3 Skin friction

The mean wall shear stress along the blade is shown as well in Figure 3. An interesting observation concerns the high Reynolds subsonic case: the flow is already relatively chaotic in the TE region

For all cases, the skin friction decreases in the nose part, up to the separation, and then a slight increase is seen close to the TE. A significant shift between the subsonic and transonic cases may be seen. The latter is explained by the shift in velocity peak at higher Mach numbers. In the subsonic case, there is a reattachment close to the TE, while it is less clear in the transonic case. In the low Reynolds choked case, the skin fric-

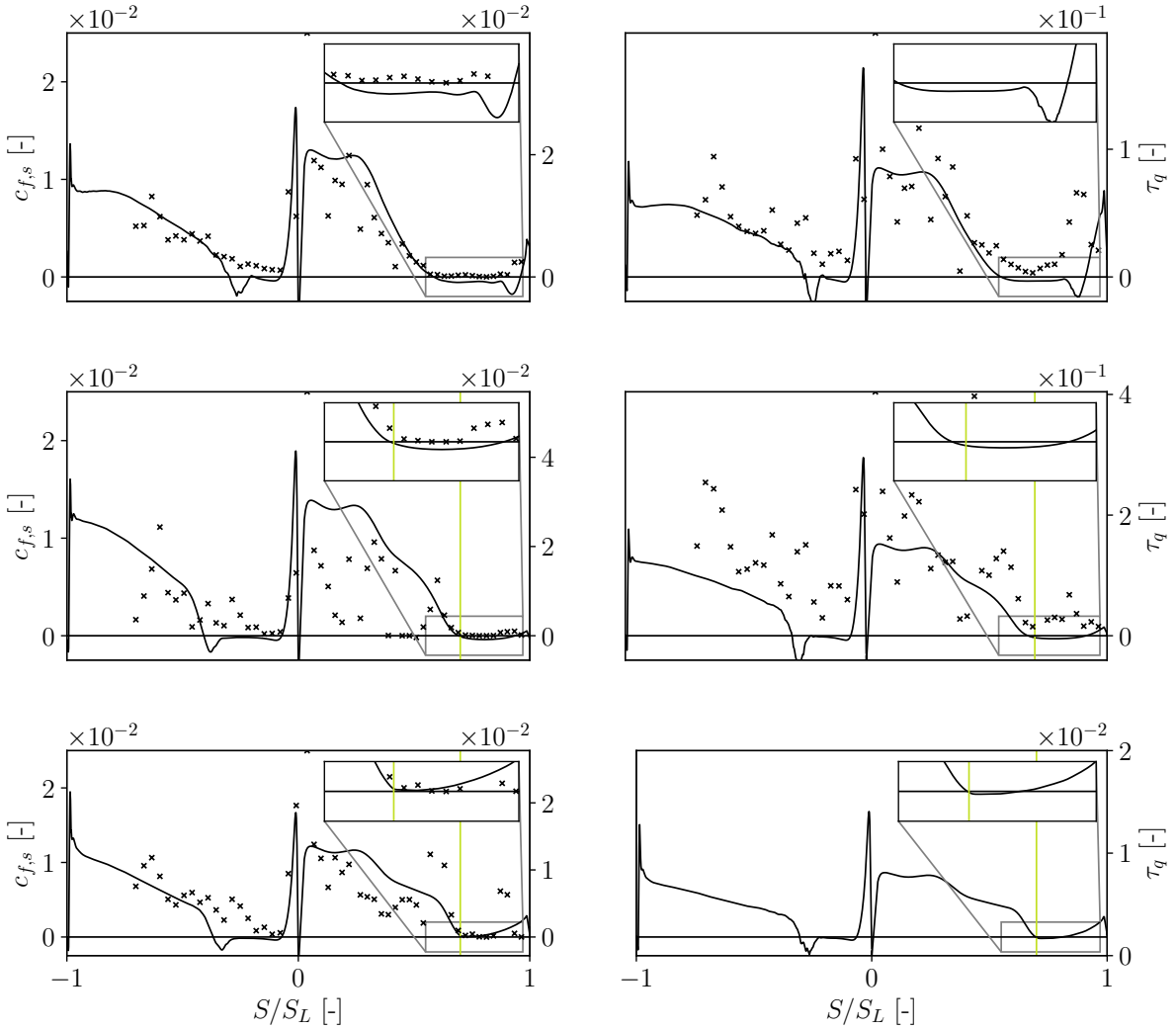

Figure 5: Time and spanwise averaged skin friction distributions along PS (negative S/S_L) and SS (positive S/S_L) for $\mathrm{Re}_{s,out} = 70 \times 10^3$ to 120×10^3 from left to right, respectively, and $M_{s,out} = 0.7$, 0.9, 0.95 (resp. 0.96) from top to bottom, respectively. The averaged shock location is depicted by a yellow vertical line.

tion reaches low values but never negative values, indicating that the BL remains attached to the blade surface. This may be explained by the smaller pressure rise for these conditions, *i.e.*, as discussed earlier, the shock restricts the pressure gradient on a smaller portion of the blade such that the momentum deficit is smaller before the shock and the BL does not separate. Besides, increasing the Reynolds number in the subsonic case allows the flow to fully reattach before TE, as shown by the relatively high values of wall shear stress at TE. This confirms the early observations made based on the Schlieren and the isentropic Mach number distribution. Again, the effect on increasing the Reynolds number is more felt at low Mach number. At high Reynolds and transonic conditions, a separation is noticeable; this is not necessarily in contradiction with the experiments as the latter only indicate the absolute values of the shear stress, whereas these are relatively low.

On the PS, in accordance to previous discussions, a small separation bubble is observed which is smaller in the subsonic case than in the higher Mach number cases.

The experimental measurements show a good match in describing separation in the post-shock separation region, although very oscillating elsewhere. This comparison between the numerical skin friction on the one hand and the experimental quasi-wall shear stress is however only qualitative as the latter does not exactly physically corresponds to the wall shear stress. However, note that the values of τ_q are non-zero in the region of the TE which indicates a reattached flow in this region, aligning with previous observations. Note that turbulence injection at the inlet, as in experiments, will probably shorten the separation bubbles (see [16]).

3.4 Boundary layer

Figure 6 displays the computed time-averaged velocity profiles in the BL all along the blade. Separation leads to inflection points in the profiles, subjecting the flow to inflectional instability and Kelvin-Helmholtz (KH) rollups. The separation bubble along the PS is visible for all cases, starting soon

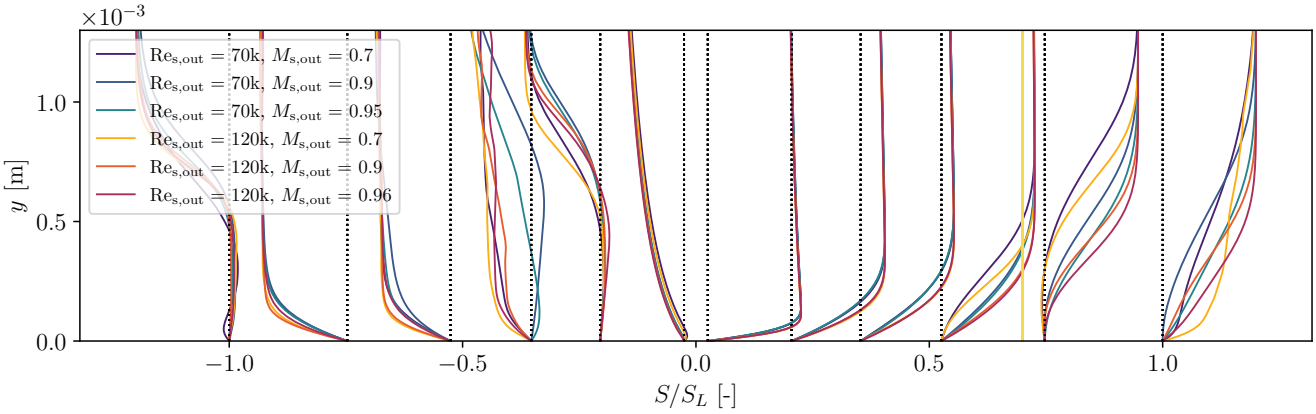

Figure 6: Time and spanwise averaged velocity profiles in the BL at different locations along the PS (negative S/S_L) and along the SS (positive S/S_L) for $\mathrm{Re}_{s,out} = 70 \times 10^3$ to 120×10^3, and $M_{s,out} = 0.7$, 0.9, 0.95 (resp. 0.96). The averaged shock location is represented by a yellow vertical line.

after the LE and reattaching before mid-chord. The bubble is thicker for higher Mach numbers and thinner for higher Reynolds numbers, as discussed earlier. In other words, reattachment is faster at subsonic and at high Reynolds conditions.

Separation on the SS can be seen for subsonic and transonic cases. In the transonic case, the bubble is shifted downstream, which let a smaller distance for transition to develop. Note that the region of separation for this case matches with the average shock location. Even though there is no separation on average in the choked cases, inflection points in the velocity profiles indicate presence of inflectional instabilities.

At higher Reynolds number, in subsonic conditions, one again can see the flow reattachment before the TE, indicated by a fuller velocity profile for this case, which is in line with previous observations.

Figure 7 shows the evolution of the integral parameters, *i.e.*, the displacement, momentum loss and kinetic energy loss (see Lieblein and Roudebush [50]) thicknesses, respectively,

$$\delta^* = \int_0^\infty \left(1 - \frac{\rho u}{\rho_e u_e}\right) \mathrm{d}y, \tag{1}$$

$$\theta = \int_0^\infty \frac{\rho u}{\rho_e u_e}\left(1 - \frac{u}{u_e}\right) \mathrm{d}y, \tag{2}$$

$$k = \int_0^\infty \frac{\rho u}{\rho_e u_e}\left(1 - \frac{u^2}{u_e^2}\right) \mathrm{d}y, \tag{3}$$

where u is the BL tangential velocity, ρ_e is the local free stream density and u_e the corresponding free stream velocity.

Along the PS, post-separation displacement thickness significantly grows, with lower values for the subsonic case. The momentum thickness growth follows however a delayed trajectory compared to the latter, due to the multiplication by the u/U_e term in the expression of θ. The shape factors initially follow the displacement thicknesses trends. As the latter decreases, the momentum thickness aligns closer to it, signifying the onset on transition. In the region of reattachment, H falls below 2, reaching approximately 1.4, indicating a turbulent flow, which is in line with Mayle [2] and Hatman and Wang [12]. Post-reattachment, H grows, reaching values around 2 at the TE, indicating reverse transition due to the favorable pressure gradient [2, 12].

Along the SS, the delayed growth of the momentum thickness compared to the displacement thickness is also observed, due to the same reason. For all cases, the shape factor increases before reaching a maximum value before the TE region. The latter maxima are reached soon after the shock for the transonic and choked cases. Typical turbulent values of the shape factor, *i.e.*, around 1.4, are never observed, except for the high Reynolds subsonic case, for which the scatter is due to a lack of convergence. Globally, the relatively large displacement and momentum thicknesses characterizing the SS BL at the TE are expected to be related to large losses in the wake, as the work of Denton [23] highlights.

Globally, the relatively large displacement and momentum thicknesses characterizing the SS BL at the TE are expected to be related to large losses in the wake, as the work of Denton [23] highlights.

Increasing the Reynolds number does not have important effect. However, in the subsonic case the relaminarisation seems more developed. Besides, high Reynolds curves show more oscillatory behavior than their low Reynolds counterparts.

3.5 Wake and losses

Figure 8 shows the magnitude of the vorticity, computed as

$$||\boldsymbol{\omega}|| = ||\boldsymbol{\nabla} \times \mathbf{u}|| \tag{4}$$

in the TE and wake region. First, note that the contours in the TE and base region support our previous observations concerning separation, transition and reattachment, *i.e.*, the onset on transition is reached in all case, with a more developed transition for subsonic cases, and fully turbulent flow for the subsonic high Reynolds case.

Furthermore, the flow is more chaotic in subsonic conditions, with unstable rows of vortices in the Karman street. In transonic conditions, the base flow shows a large separation

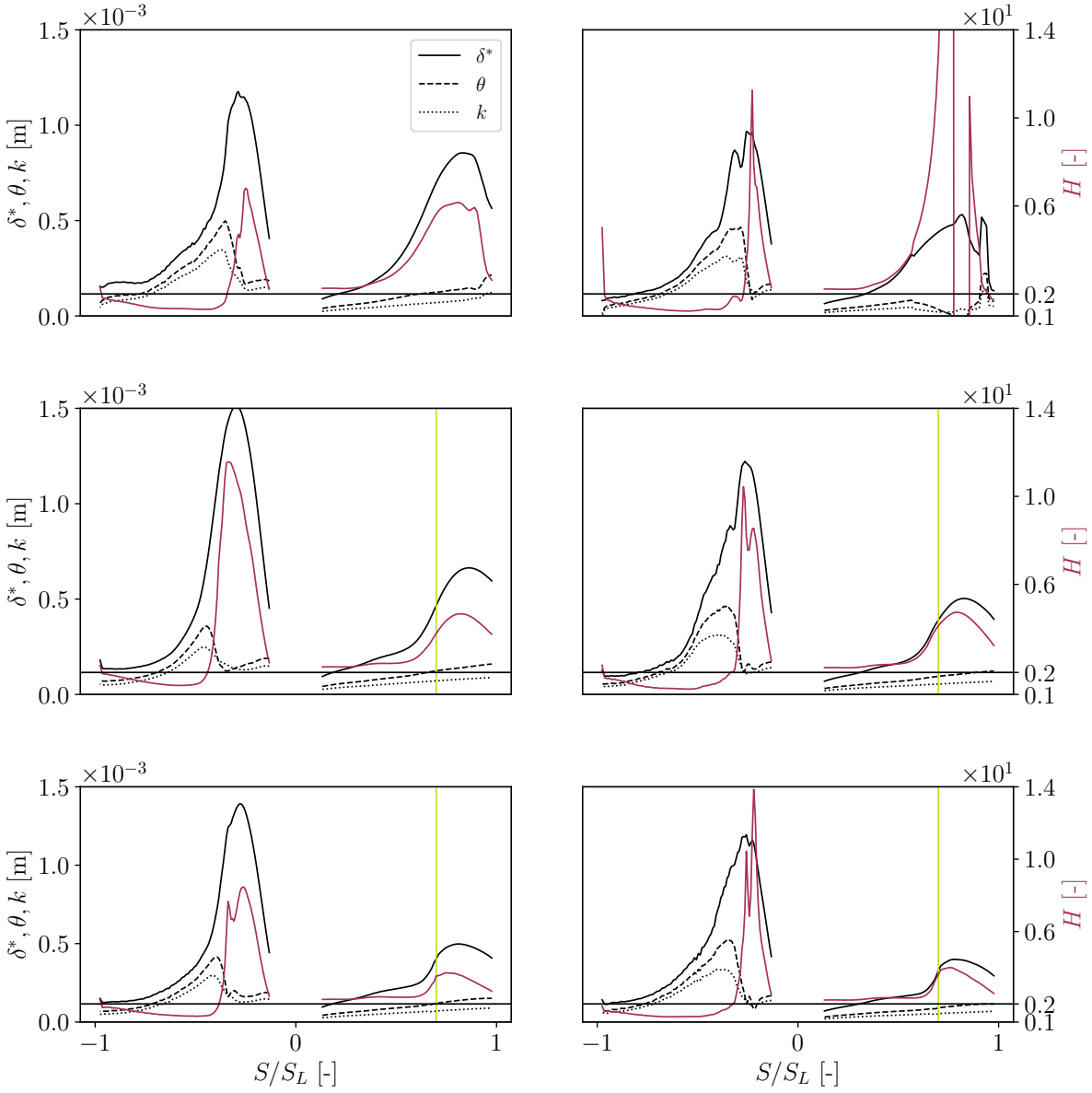

Figure 7: Time and spanwise averaged displacement, momentum, energy thicknesses and shape factor in the BL for $\mathrm{Re}_{s,out} = 70 \times 10^3$ to 120×10^3 from left to right, respectively, and $M_{s,out} = 0.7$, 0.9, 0.95 (resp. 0.96) from top to bottom, respectively. The averaged shock location is depicted by a yellow vertical line.

followed by vortex shedding and its vortex street. At these conditions, the rows of vortices are more regularly staggered. The turbulence decay is slower as the Mach number increases, and as the Reynolds number decreases. This large separation in the base region seems to shorten in the choked case.

The differences in TE base flow behavior depending on the Mach number are the opposite of results of Vagnoli et al. [25]. Indeed, the base flow does not show large separation at moderate Reynolds subsonic conditions, *i.e.*, the vortex sheds and detaches directly in the TE region. Increasing the Mach number towards high subsonic and transonic regime leads to a steady separated base flow, followed by a large vortex shedding region. Note that in this case, increasing the Reynolds number tends to shorten the recirculation region. Increasing the Mach number further gives back a shorter recirculation region followed again by the vortex shedding. Figure 3 allows to see that the shock interacts with base flow in choked conditions which may have an effect on the extent of the base flow.

Finally, Figure 9 provides the pressure losses at the downstream location $x/c_{ax} = 1.5$. It can be seen that losses increase with increasing Mach number and decrease with increasing Reynolds number, which was expected from Vera et al. [17]. With respect to the measurements, the losses seem to be too concentrated, in line with the differences in the separated region where we expect transition to occur earlier in the case of turbulent inlet flow.

Although other reasons may explain these, the observed discrepancies may probably come from the differences in in-

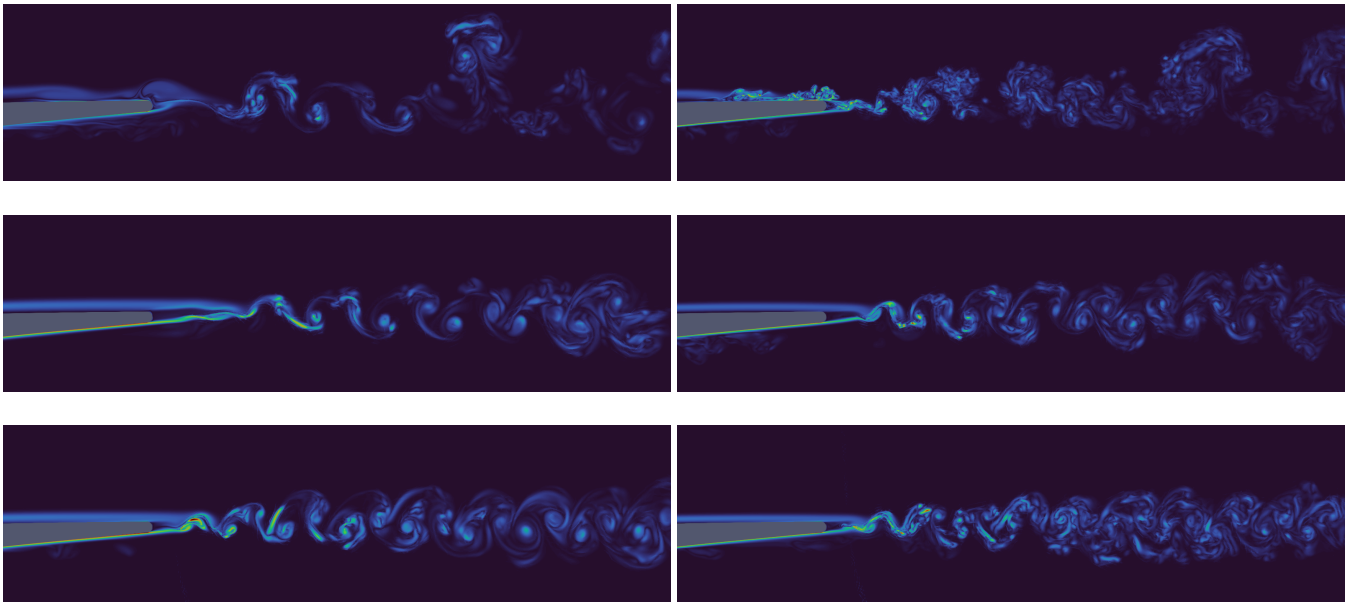

Figure 8: Snapshots of the vorticity contours in the base / wake region for $\mathrm{Re}_{\mathrm{s,out}} = 70 \times 10^3$ to 120×10^3 from left to right, respectively, and $M_{\mathrm{s,out}} = 0.7, 0.9, 0.95$ (resp. 0.96) from top to bottom, respectively.

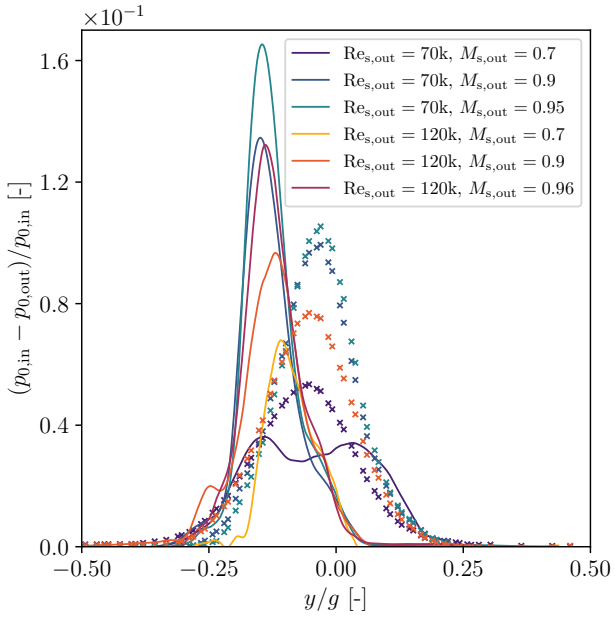

Figure 9: Time and spanwise averaged total pressure losses along the pitchwise direction at $x/c_{\mathrm{ax}} = 1.5$ for $\mathrm{Re}_{\mathrm{s,out}} = 70 \times 10^3$ to 120×10^3, and $M_{\mathrm{s,out}} = 0.7,\ 0.9,\ 0.95$ (resp. 0.96). Experimental data are represented by cross ($\times$ symbols).

let turbulence between numerical setup and experiments. Besides, the shape of the low and high Reynolds subsonic cases indicate a lack of convergence for these cases. The latter issue is due to a more chaotic behavior of the wake for these cases which requires more through flow times to be converged.

4 Conclusions

The current paper discusses a first step in the numerical investigations into the effects of compressibility on separation and transition on a high speed low pressure turbine cascade, measured in the SPLEEN project.

To this effect, two Reynolds numbers and three Mach numbers, corresponding to the experimental campaign, are investigated. In order to distinguish the role of inlet turbulence and upstream running acoustic waves, issued from the wake, clean and turbulent conditions are currently undertaken. This paper discusses the first results obtained with clean conditions, whereas computations with inlet turbulence are ongoing.

The impact of compressibility is clearly noticeable. First of all, the separation on the suction side is suppressed in choked conditions. Choking furthermore prevents the acoustic waves, that otherwise dominate the passage flow, to propagate from the wake upstream and perturb the suction side boundary layer, whereas the separation and transition on the pressure side develop independently.

The results show reasonable agreement with the experiments, but some notable differences remain in particular at subsonic conditions. This includes the presence of a separation bubble at the PS, and a modified separation bubble at the SS trailing edge. These lead to slight modifications in the pressure distribution, which are probably attributable to the absence of inlet turbulence; the currently ongoing studies with inlet turbulence seem to corroborate this hypothesis.

Acknowledgements

This work was supported by computational resources made available by the Consortium des Équipements de Calcul Intensif (CÉCI) funded by the F.R.S.-FNRS and the Walloon

Region, on Lucia, the Tier-1 supercomputer of the Walloon Region, infrastructure funded by the Walloon Region under the grant agreement n°1910247. Data was obtained experimentally during the CleanSky II "SPLEEN" project, financed by the European Union Horizon 2020 programme. We also thank Safran for their valuable collaboration.

Nomenclature

c	true chord
$c_{f,s}$	skin friction coefficient
H	shape factor
k	pseudo-energy thickness
M	Mach number
$n+$	wall units in the normal direction to the blade
S	sponge layer source term / curvilinear coordinate
$s+$	wall units in the tangential direction to the blade
u	instantaneous solution / tangential velocity in the BL
U_e	local free stream velocity in the BL
y	normal distance to the blade in the boundary layer / pitch coordinates in the wake
Re	Reynolds number

Greek symbols

$\boldsymbol{\omega}$	vorticity
δ^*	displacement thickness
ρ_e	local fluid density in the BL
θ	momentum thickness

Subscripts

L	blade curvilinear length
ax	axial
in	inlet
out	outlet
s	isentropic

Superscripts

-	time average

Acronyms

(U)RANS	Unsteady Reynolds Averaged Navier-Stokes
BDF2	Second Order Backward Difference
BL	Boundary Layer
DGM	discontinuous Galerkin method
DNS	Direct Numerical Simulation
GMRES	Generalized Minimal Residual
GTF	geared turbofan
HPC	High Performance Computing
HSLPT	high-speed low pressure turbine
LE	Leading Edge
LES	Large Eddy Simulation
LP	low pressure
LPT	low pressure turbine
SIPDG	Symmetric Internal Penalty Discontinuous Galerkin
SS	Suction Side
TE	Trailing Edge
TKE	Turbulent Kinetic Energy

References

[1] J. Kurzke. “Fundamental Differences Between Conventional and Geared Turbofans”. In: *ASME Turbo Expo 2009: Power for Land, Sea, and Air*. Orlando, Florida, USA, 2009.

[2] R. E. Mayle. “The Role of Laminar-Turbulent Transition in Gas Turbine Engines”. In: *Proceedings of the International Gas Turbine and Aeroengine Congress and Exposition*. Orlando, FL, USA, 1991.

[3] R. Pacciani, M. Marconcini, A. Arnone, and F. Bertini. “A CFD Study of Low Reynolds Number Flow in High Lift Cascades”. In: *ASME Turbo Expo 2010: Power for Land, Sea, and Air*. Glasgow, UK, 2010.

[4] K. Cobley, N. Coleman, G. Siden, and N. Arndt. “Design of New Three Stage Low Pressure Turbine for the BMW Rolls-Royce BR715 Turbofan Engine”. In: *Proceedings of the International Gas Turbine and Aeroengine Congress and Exhibition*. Orlando, Florida, USA, 1997.

[5] E. M. Curtis, H. P. Hodson, M. R. Banieghbal, J. D. Denton, R. J. Howell, and N. W. Harvey. “Development of Blade Profiles for Low-Pressure Turbine Applications”. In: *Journal of Turbomachinery* 119.3 (1997), pp. 531–538. DOI: 10.1115/1.2841154.

[6] F. Haselbach, H.-P. Schiffer, M. Horsman, S. Dressen, N. Harvey, and S. Read. “The Application of Ultra High Lift Blading in the BR715 LP Turbine”. In: *Journal of Turbomachinery* 124.1 (2002), pp. 45–51. DOI: 10.1115/1.1415737.

[7] R. J. Howell, H. P. Hodson, V. Schulte, R. D. Stieger, H.-P. Schiffer, F. Haselbach, and N. W. Harvey. "Boundary Layer Development in the BR710 and BR715 LP Turbines—The Implementation of High-Lift and Ultra-High-Lift Concepts". In: *Journal of Turbomachinery* 124.3 (2002), pp. 385–392. DOI: 10.1115/1.1457455.

[8] X. F. Zhang, H. P. Hodson, and N. W. Harvey. "Unsteady boundary layer studies on ultra-high-lift low-pressure turbine blades". In: *Proceedings of the Institution of Mechanical Engineers, Part A: Journal of Power and Energy* 219.6 (2005). DOI: 10.1243/095765005X31207.

[9] R. J. Volino and L. S. Hultgren. "Measurements in Separated and Transitional Boundary Layers Under Low-Pressure Turbine Airfoil Conditions". In: *Journal of Turbomachinery* 123.2 (2001), pp. 189–197. DOI: 10.1115/1.1350408.

[10] R. D. Stieger. *The Effects of Wakes on Separating Boundary Layers in Low Pressure Turbines*. en. Cambridge University Press, Cambridge, UK, 2002.

[11] W. Lou and J. Hourmouziadis. "Separation Bubbles Under Steady and Periodic-Unsteady Main Flow Conditions". In: *Journal of Turbomachinery* 122.4 (2000), pp. 634–643. DOI: doi.org/10.1115/1.1308568.

[12] A. Hatman and T. Wang. "A Prediction Model for Separated-Flow Transition". In: *Journal of Turbomachinery* 121.3 (1999), pp. 594–602. DOI: 10.1115/1.2841357.

[13] R. Houtermans, T. Coton, and T. Arts. "Aerodynamic Performance of a Very High Lift Low Pressure Turbine Blade With Emphasis on Separation Prediction". In: *Journal of Turbomachinery* 126.3 (Sept. 2004), pp. 406–413. DOI: 10.1115/1.1748416.

[14] G. B. Schubauer and P. S. Klebanoff. *Contributions on the mechanics of boundary-layer transition*. Tech. rep. TR-1289. NACA, 1956.

[15] M. Dellacasagrande, D. Lengani, D. Simoni, and S. Yarusevych. "A data-driven analysis of short and long laminar separation bubbles". In: *Journal of Fluid Dynamics* 976.R3 (2023). DOI: 10.1017/jfm.2023.960.

[16] M. Dellacasagrande, D. Lengani, D. Simoni, and M. Ubaldi. "An Experimental Database for the Analysis of Bursting of a Laminar Separation Bubble". In: *International Journal of Turbomachinery Propulsion and Power* 9.3 (2024). DOI: 10.3390/ijtpp9010003.

[17] M. Vera, H. Hodson, and R. Vazquez. "THE EFFECT OF MACH NUMBER ON LP TURBINEWAKE-BLADE INTERACTION". In: *Unsteady Aerodynamics, Aeroacoustics and Aeroelasticity of Turbomachines*. 2006.

[18] M. Vera and H. Hodson. "LOW SPEED VS HIGH SPEED TESTING OF LP TURBINE BLADE-WAKE INTERACTION". In: *Proceedings of the 16th Symposium on Measuring Techniques in Transonic and Supersonic Flow in Cascades and Turbomachines*. Cambridge, UK, 2002.

[19] R. Vázquez and D. Torre. "The Effect of Mach Number on the Loss Generation of LP Turbines". In: *ASME Turbo Expo 2012: Turbine Technical Conference and Exposition*. Copenhagen, Denmark, 2012.

[20] J. Michálek, M. Monaldi, and T. Arts. "Aerodynamic Performance of a Very High Lift Low Pressure Turbine Airfoil (T106C) at Low Reynolds and High Mach Number With Effect of Free Stream Turbulence Intensity". In: *Journal of Turbomachinery* 134.6 (2012). DOI: 10.1115/1.4006291.

[21] R. Vázquez, A. Antoranz, D. Cadrecha, and L. Armañanzas. "The Influence of Reynolds Number, Mach Number and Incidence Effects on Loss Production in Low Pressure Turbine Airfoils". In: *ASME Turbo Expo 2006: Power for Land, Sea, and Air*. Barcelona, Spain, 2006.

[22] M. Börner and R. Niehuis. "Dynamics of Shock Waves Interacting With Laminar Separated Transonic Turbine Flow Investigated by High-Speed Schlieren and Surface Hot-Film Sensors". In: *Journal of Turbomachinery* 143.5 (2021). DOI: 10.1115/1.4050330.

[23] J. D. Denton. "Loss Mechanisms in Turbomachines". In: *ASME 1993 International Gas Turbine and Aeroengine Congress and Exposition*. Cincinnati, Ohio, USA, 1993.

[24] C. Sieverding and M. Manna. "A Review on Turbine Trailing Edge Flow". In: *International Journal of Turbomachinery Propulsion and Power* 5.2 (2020). DOI: 10.3390/ijtpp5020010.

[25] S. Vagnoli, T. Verstraete, B. Mateos, and C. Sieverding. "Prediction of the unsteady turbine trailing edge wake flow characteristics and comparison with experimental data". In: *Proceedings of the Institution of Mechanical Engineers, Part A: Journal of Power and Energy* 229.5 (2015). DOI: 10.1177/0957650915592074.

[26] V. Michelassi, J. Wissink, and W. Rodi. "Analysis of DNS and LES of Flow in a Low Pressure Turbine Cascade with Incoming Wakes and Comparison with Experiments". In: *Flow, Turbulence and Combustion* 69 (2002), pp. 295–329. DOI: 10.1023/A:1027334303200.

[27] V. Michelassi, L.-W. Chen, R. Pichler, and R. D. Sandberg. "Compressible Direct Numerical Simulation of Low-Pressure Turbines—Part II: Effect of Inflow Disturbances". In: *Journal of Turbomachinery* 137.071005 (July 2015). DOI: 10.1115/1.4029126.

[28] R. Pacciani, M. Marconcini, A. Arnone, and F. Bertini. "An assessment of the laminar kinetic energy concept for the prediction of high-lift, low-Reynolds number cascade flows". In: *Proceedings of the Institution of Mechanical Engineers, Part A: Journal of Power and Energy* 225.7 (2011). DOI: 10.1177/0957650911412444.

[29] N. Rosafio, G. Lopes, S. Salvadori, S. Lavagnoli, and D. A. Misul. "RANS Prediction of Losses and Transition Onset in a High-Speed Low-Pressure Turbine Cascade". In: *Energies* 16.21 (2023). DOI: 10.3390/en16217348.

[30] A. Boudin, J. Dombard, F. Duchaine, L. Gicquel, N. Odier, S. Lavagnoli, G. Lopes, L. Simonassi, and F. Safran Aircraft Engines. "Analysis of rotor/stator interactions in a high-speed low-pressure turbine cascade using Large-Eddy Simulations." In: *Proceedings of the 15th European Conference on Turbomachinery Fluid dynamics and Thermodynamics*. Budapest, Hungary, 2023.

[31] G. Lopes, L. Simonassi, and S. Lavagnoli. "Impact of Unsteady Wakes on the Secondary Flows of a High-Speed Low-Pressure Turbine Cascade". In: *International Journal of Turbomachinery, Propulsion and Power* 8.4 (2023). DOI: 10.3390/ijtpp8040036.

[32] G. Lopes, L. Simonassi, A. F. M. Torre, and S. Lavagnoli. "Instrumentation Interference in a Transonic Linear Cascade". In: *Journal of Physics: Conference Series, Volume 2511, XXVI Biennial Symposium on Measuring Techniques in Turbomachinery (MTT2622)*. Pisa, Italy, 2022.

[33] G. Lopes, L. Simonassi, and S. Lavagnoli. "Time-Averaged Aerodynamics of a High-Speed Low-Pressure Turbine Cascade With Cavity Purge and Unsteady Wakes". In: *Journal of Turbomachinery* 146.2 (2024). DOI: 10.1115/1.4063878.

[34] L. Simonassi, G. Lopes, and S. Lavagnoli. "Effects of Periodic Incoming Wakes on the Aerodynamics of a High-Speed Low-Pressure Turbine Cascade". In: *International Journal of Turbomachinery, Propulsion and Power* 8.3 (2023). DOI: 10.3390/ijtpp8030035.

[35] S. Lavagnoli, G. Lopes, L. Simonassi, and A. F. M. Torre. *SPLEEN - High Speed Turbine Cascade – Test Case Database*. 2024. DOI: 10.5281/zenodo.13712768.

[36] M. Borbouse, G. Lopes, S. Lavagnoli, M. Rasquin, and K. Hillewaert. "Analysis of separation and transition on a novel high-speed low pressure turbine cascade". In: *Proceedings of the Cambridge Unsteady Flow Symposium*. Cambridge, UK, 2024.

[37] M. Borbouse, G. Lopes, S. Lavagnoli, M. Rasquin, and K. Hillewaert. "Boundary layer stability and shock interactions in a high speed low pressure turbine cascade". In: *Proceedings of the 14th Direct and Large Eddy Simulation*. Erlangen, Germany, 2024.

[38] M. Okada, L. Simonassi, G. Lopes, and S. Lavagnoli. "Compressible Direct Numerical Simulation of Low-Pressure Turbines—Part II: Effect of Inflow Disturbances". In: *ASME Turbo Expo 2023: Turbomachinery Technical Conference and Exposition*. Boston, Massachusetts, USA, 2023.

[39] K. Hillewaert. *Development of the discontinuous Galerkin method for high-resolution, large scale CFD and acoustics in industrial geometries*. Presses universitaires de Louvain, 2013.

[40] C. Carton de Wiart, K. Hillewaert, M. Duponcheel, and G. Winckelmans. "Assessment of a discontinuous Galerkin method for the simulation of vortical flows at high Reynolds number". In: *International Journal for Numerical Methods in Fluids* 74.7 (2014), pp. 469–493.

[41] K. Hillewaert, J. Cagnone, S. Murman, A. Garai, Y. Lv, and M. Ihme. "Assessment of high-order DG methods for LES of compressible flows". In: *Proceedings of the Center for Turbulence Research Summer Program*. 2016.

[42] C. C. de Wiart, K. Hillewaert, and P. Geuzaine. "DNS of a low pressure turbine blade computed with the discontinuous Galerkin method". In: *Turbo Expo: Power for Land, Sea, and Air*. Vol. 44748. American Society of Mechanical Engineers. 2012, pp. 2101–2111.

[43] C. Carton de Wiart, K. Hillewaert, E. Lorriaux, and G. Verheylewegen. "Development of a discontinuous Galerkin solver for high quality wall-resolved/modelled DNS and LES of practical turbomachinery flows on fully unstructured meshes". In: *Turbo Expo: Power for Land, Sea, and Air*. Vol. 56642. American Society of Mechanical Engineers. 2015, V02BT39A035.

[44] M. Rasquin, J.-F. Thomas, P. Bechlars, M. Franke, K. Hillewaert, et al. "Direct numerical simulations of airfoil cascades for the improvement of turbulence models through database generation". In: *15th European Conference on Turbomachinery Fluid dynamics & Thermodynamics*. ETC. 2023.

[45] J.-S. Cagnone, M. Rasquin, K. Hillewaert, and S. Hiernaux. "Large eddy simulation of a low pressure compressor cascade at high incidence". In: *12th European Conference on Turbomachinery Fluid dynamics & Thermodynamics*. ETC. 2017.

[46] C. Geuzaine and J.-F. Remacle. "Gmsh: A 3-D finite element mesh generator with built-in pre- and post-processing facilities". In: *International Journal for Numerical Methods in Engineering* 79.11 (2009), pp. 1309–1331. DOI: 10.1002/nme.2579.

[47] M. Rasquin, A. Bauer, and K. Hillewaert. "Scientific post hoc and in situ visualisation of high-order polynomial solutions from massively parallel simulations". In: *International Journal of Computational Fluid Dynamics* 33.4 (2019), pp. 171–180. DOI: 10.1080/10618562.2019.1618453.

[48] M. Gaster. “The structure and behaviour of separation bubbles”. In: *Aeronautical Research Council Reports & Memoranda*. 1967.

[49] M. Gaster. “LAMINAR SEPARATION BUBBLES”. In: *IUTAM Symposium on Laminar-Turbulent Transition*. Ed. by R. Govindarajan. Dordrecht: Springer Netherlands, 2006, pp. 1–13. DOI: 10.1007/1-4020-4159-4_1.

[50] S. Lieblein and W. H. Roudebush. *Theoretical loss relations for low-speed two-dimensional-cascade flow*. Tech. rep. TN-3662. NACA, 1956.